Accidental persistent spin textures in the proustite mineral family

Sean Koyama [*] and James M. Rondinelli [†]
Department of Materials Science and Engineering, Northwestern University, Evanston, Illinois 60208, USA

(Received 31 August 2022; revised 21 December 2022; accepted 20 January 2023; published 31 January 2023)

Persistent spin textures (PSTs) in momentum space have the potential to enable spintronic devices which are currently limited by spin lifetimes in nonmagnetic spin-orbit coupled materials. We perform a first-principles study on the proustite mineral family, Ag_3BQ_3 (B = As, Sb; Q = S, Se), and show these chalcogenides exhibit nonsymmetry-protected PSTs, which we refer to as symmetry-assisted PSTs. Chemical substitution can be used to tune the PST quality and properties, e.g., spin lifetime, and we find that a Rashba anisotropy criterion correlates with the PST area and spin lifetime for two of the three proustites examined. Last, we show that a first-order effective SOC Hamiltonian, often used in two-dimensional systems, is insufficient to describe the PST state in all proustites, suggesting that higher order models are necessary to fully describe PSTs in bulk three-dimensional materials.

DOI: 10.1103/PhysRevB.107.035154

I. INTRODUCTION

Nonmagnetic materials with unidirectional spin-momentum locking, or a persistent spin texture (PST), exhibit electrical transport properties useful for spintronic applications [1,2]. In particular, a PST at the Fermi level of a conducting system enables the persistent spin helix (PSH) transport mode in which an electron's spin precesses around a fixed axis as it moves through the material. This mode is immune to decoherence from some low-temperature scattering mechanisms. PST formation requires the presence of strong spin-orbit coupling (SOC) combined with inversion symmetry breaking. This combination produces SOC-derived band splitting and is responsible for the well-known Rashba and Dresselhaus splittings and spin textures. In contrast to the aforementioned spin textures, a PST consists of unidirectionally aligned spins which are momentum independent. This feature has been reported theoretically and observed experimentally in quantum well structures, 2D materials, and at interfaces [3–5]. PSTs were recently theorized to exist in bulk three-dimensional (3D) systems exhibiting nonsymmorphic symmetries [6] along with strong SOC and broken inversion symmetry, and several bulk materials, primarily ferroelectric oxides, have since been predicted to host a PST [7–9].

The 3D PST materials predicted thus far all exhibit a symmetry-protected PST (SP-PST), also known as a type-I PST [10,11], which is enforced through crystalline symmetries. Recently, mirror symmetries were shown to be the key ingredient for forming a SP-PST [9]. The symmetry protection, however, is a sufficient but not necessary component to form a PST in bulk materials—it is possible to tune the strength of SOC parameters to produce an "accidental" or type-II PST that is not enforced by symmetry [11]. In this paper, we perform electronic structure simulations and model Hamiltonian calculations to show that the proustites (Ag_3BQ_3), a family of silver chalcogenide minerals, exhibit type-II PSTs. By looking beyond symmetry-constrained PSTs and examining a family with high chemical tunability, we uncover symmetry-assisted PSTs in the proustite family. Our study expands the number of polar compounds that can exhibit high-quality PSTs and spin helices.

II. MATERIALS AND METHODS

A. Proustite family

The proustite family consists of three compounds in space group $R3c$: The namesake mineral Ag_3AsS_3, as well as Ag_3SbS_3 and Ag_3AsSe_3. The former two are naturally occurring minerals and all three have been experimentally synthesized as bulk single crystals [12–14]. The crystal structure of Ag_3AsS_3 [Fig. 1(a)] consists of AsS_3 pyramids connected along the c axis by Ag-S chains [Fig. 1(b)] which are generated by a 3_1 screw axis. Owing to the c-glide plane, two sublattices of the AsS_3 pyramids and chains exist, where each sublattice is chiral but of opposite handedness from the other, resulting in an achiral crystal. The isostructural variants are similar (see Table I and Ref. [15]).

B. Computational details

Density functional theory (DFT) calculations were performed using the VIENNA *AB INITIO* SIMULATION PACKAGE [16–18] with a plane-wave cutoff of 350 eV and projector-augmented wave (PAW) pseudopotential [19,20] with Ag 5s and 4d, As 4s and 4p, Sb 5s and 5p, S 3s and 3p, and Se 4s and 4p electrons as valence states. We utilized the PBEsol exchange-correlation functional with SOC included, unless specified otherwise [21,22]. The Brillouin zone is sampled with a $4 \times 4 \times 4$ k-point mesh and integrations are performed with the tetrahedon method [23].

[*] skoyama@anl.gov
[†] jrondinelli@northwestern.edu

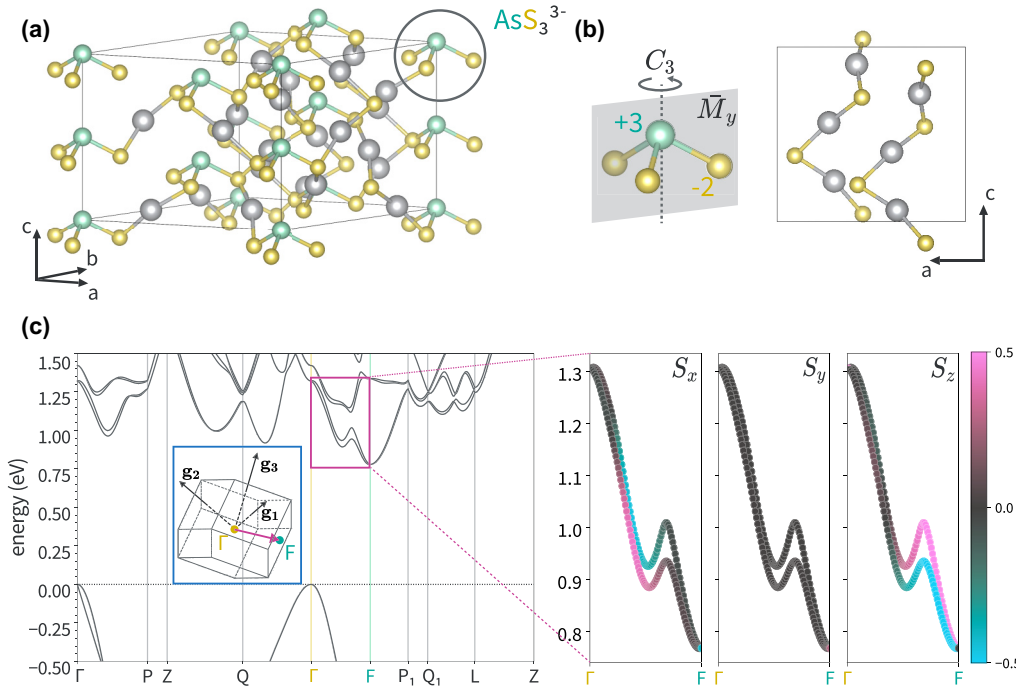

FIG. 1. (a) Crystal structure of Ag_3AsS_3 in the hexagonal setting (b) comprises two building blocks: AsS_3 pyramids linked together by Ag-S chains. (c) The band structure of Ag_3AsS_3 showing the valence band minimum (VBM) and conduction band maximum (CBM) at Γ and F, respectively. Inset: The Brillouin zone of the material with special points of interest. Zoomed: Lowest two conduction bands in the $F \rightarrow \Gamma$ path with projected spin character (color mapped).

Structures were relaxed until forces were below 1×10^{-4} eV Å^{-1}. Electric polarizations were calculated using the Berry phase method [24]. The HSE06 hybrid functional [25] was used for accurate band-gap calculations and dense k-point meshes were constructed for non-self-consistent field band dispersion and spin-texture calculations. The Atomic Simulation Environment was used to aid calculations and post-processing [26]. The LOBSTER code was used for parsing density of states calculations [27–30] and VESTA [31] was used for structure visualization.

C. Spin lifetime calculations

To compute the spin lifetime, we follow previous analysis of bulk PST systems [9] and the Keldysh formulation of the nonequilibrium Green's function for the spin transport equation (using units of $\hbar = 1$) [32]. The following derivation follows closely that in Ref. [32]:

$$\partial_t \hat{g} + \nabla_{\mathbf{R}} \cdot \left\{ \frac{1}{2}\hat{\mathbf{V}}, \hat{g} \right\} + i[\mathbf{B}(\mathbf{k}) \cdot \hat{\sigma}, \hat{g}] + \frac{\hat{g}}{\tau} = \frac{\hat{\rho}}{\tau}, \qquad (1)$$

where $\hat{g}(\theta, \mathbf{R})$ is the distribution function; $\hat{\rho}(\mathbf{R})$ is the density operator (which is the distribution function integrated over θ),

TABLE I. Computed lattice parameters (Å) and c/a ratios of the proustite family members in their hexagonal setting.

Compound	a	c	c/a ratio
Ag_3AsS_3	10.6	8.74	0.825
Ag_3SbS_3	10.6	9.10	0.858
Ag_3AsSe_3	11.3	8.35	0.739

$\hat{\mathbf{V}}$ is the velocity operator $\partial_k \mathcal{H}$, $\mathbf{B}$ is the effective SOC field, $\hat{\sigma}$ is the vector of Pauli matrices, and τ is the scattering time of the dominant scattering mechanism.

We note that Eq. (1) relies on several assumptions, one of which is that the relevant low-energy electronic structure is two-dimensional. We apply this equation to our material as a point of comparison to previous studies which use the same formalism; however, we acknowledge that the result is only physical if the material is synthesized in a thin film geometry or such that the carrier density is confined effectively to two dimensions through, for example, electrostatic gating or δ-doping approaches. We also neglect the temperature-dependent effects, assuming transport at 0 K and take $\tau = 1$ ps as per Ref. [9] to allow for direct comparison with prior results.

We solve Eq. (1) by performing a Fourier transform of $\partial_t \rightarrow -i\omega$ and $\partial_{x,y,z} \rightarrow iq_{x,y,z}$. By arranging the terms into a matrix equation in the Pauli matrix basis where $\hat{g} = g_c\sigma_0 + g_x\sigma_x + g_y\sigma_y + g_z\sigma_z$ and letting $\tilde{\Omega} = 1 - i\omega\tau + i\mathbf{q} \cdot \mathbf{v}\tau$, we arrive at $\hat{\rho} = D\hat{\rho}$, where

$$D = \int \frac{d\theta}{2\pi} \begin{bmatrix} \tilde{\Omega} & i\alpha_{yx}q_y\tau & i\alpha_{xy}q_x\tau & i\alpha_{yz}q_y\tau \\ i\alpha_{yx}q_y\tau & \tilde{\Omega} & 2\alpha_{yz}k_y\tau & -2\alpha_{xy}k_x\tau \\ i\alpha_{xy}q_x\tau & -2\alpha_{yz}k_y\tau & \tilde{\Omega} & 2\alpha_{yx}k_y\tau \\ i\alpha_{yz}q_y\tau & 2\alpha_{xy}k_x\tau & -2\alpha_{yx}k_y\tau & \tilde{\Omega} \end{bmatrix}^{-1}, \qquad (2)$$

and we have substituted the allowed first-order α_{ij} SOC terms for our proustites.

TABLE II. Experimental (Exp.) and DFT band gaps (E_g) of the proustite-structured compounds in units of eV.

Material	E_g(Exp.)	E_g (DFT)		
		PBEsol	+SOC	+SOC+HSE06
Ag_3AsS_3	1.99 [33]	0.782	0.767	1.57
Ag_3SbS_3		0.372	0.361	1.07
Ag_3AsSe_3		0.446	0.413	1.14

For the dynamical equation to have nontrivial solutions, the determinant of $(I - D)$ must be zero. Solving the determinant equation thus gives the eigenfrequencies of the dynamical equation ω, which leads to the characteristic timescale or spin lifetime $\tau_s = 1/i\omega$ for the damped PSH. A more useful quantity than τ_s for relative comparison is τ_s/T_{PSH}, the ratio of the spin lifetime to the PSH period. The PSH period was computed with $T_{\mathrm{PSH}} = \pi/(k_F\,\alpha_{\mathrm{eff}})$, using the Fermi velocity k_F/m and the PSH length $\pi/(m\,\alpha_{\mathrm{eff}})$ from our DFT calculations. The Fermi wave vector k_F was determined by integrating the density of states to a carrier density of $n = 1 \times 10^{19}\,\mathrm{cm}^{-3}$ and taking the k_F value along the PST direction. Equation (2) was implemented in MATHEMATICA and the Wolfram Script code is available at Ref. [15].

III. RESULTS AND DISCUSSION

A. Electronic structure

Ag_3AsS_3 is a semiconductor with an experimental band gap of $E_g = 1.99\,\mathrm{eV}$ [33]. Its computed band gap at the DFT-PBEsol level is significantly smaller than the experimental value (Table II). The inclusion of SOC reduces the computed band gap further; however, the HSE06 functional with SOC predicts a value of $E_g = 1.57\,\mathrm{eV}$, which is closer to the experimental value. Thus, PBEsol underestimates the band gap by approximately 61%, while the hybrid functional underestimates it by 21%. Although experimental band gaps are not available for the other proustite variants, their computed band gaps follow similar trends with respect to functional choice.

The DFT-computed band structure with SOC [Fig. 1(c)] reveals an indirect band gap with its valence band maximum (VBM) at Γ and its CBM at F $(\frac{1}{2}, -\frac{1}{2}, 0)$. This is consistent with prior experimental reports of an indirect band gap [33]. The lowest conduction band in the $F \to \Gamma$ path shows strong spin polarization near the F point with $s_y \approx 0$ [Fig. 1(c)]. This suggests that an interesting spin texture may exist near the F point; we show later that this is a PST.

The orbital-projected density of states shows that the valence band is made up of primarily hybridized Ag 4d and S 3p orbitals [Fig. 2(a)], while the conduction band consists of hybridized As 4p and S 3p with Ag 5s orbitals. The band edges are dominated by S and As p orbitals. To elucidate the nature of the frontier orbitals forming these bands, we construct a molecular orbital (MO) diagram of the AsS_3 molecular units with their p orbitals as basis functions [Fig. 2(a), inset]. Since the AsS_3 unit has C_{3v} symmetry, the σ interactions form pairs of bonding and antibonding a_1 and e orbitals as deduced from the character table [Fig. 2(b)]. The remaining S p orbitals remain nonbonding with the As orbitals and form the valence band through interactions with the Ag d orbitals. The MO description accurately predicts the orbital characters at the

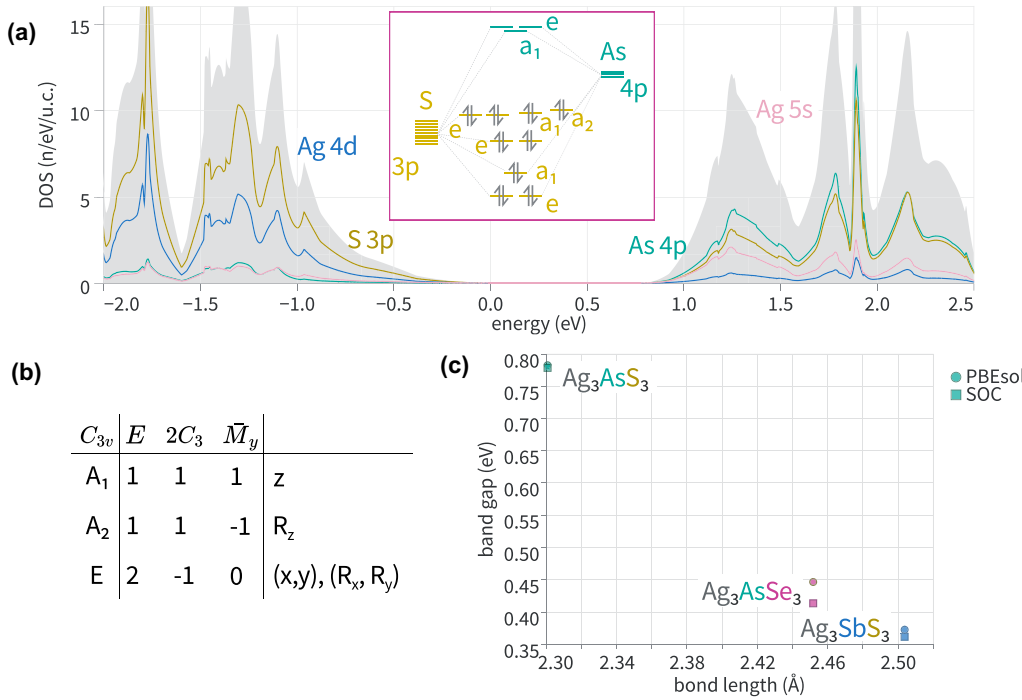

C_{3v}	E	$2C_3$	$\bar{M}_y$	
A_1	1	1	1	z
A_2	1	1	-1	R_z
E	2	-1	0	(x,y), (R_x, R_y)

FIG. 2. (a) Orbital projected density of states (DOS) near the Fermi level. The inset shows the molecular orbital diagram of the AsS_3^{3-} unit in Ag_3AsS_3 which explains the origin of the As and S orbital characters at the band edges. (b) Character table of the C_{3v} point group of AsS_3^{3-}. (c) Band-gap dependence on As-S bond length in the proustite family showing that shorter bond lengths (stronger As-S interactions) are linearly correlated with larger band gaps.

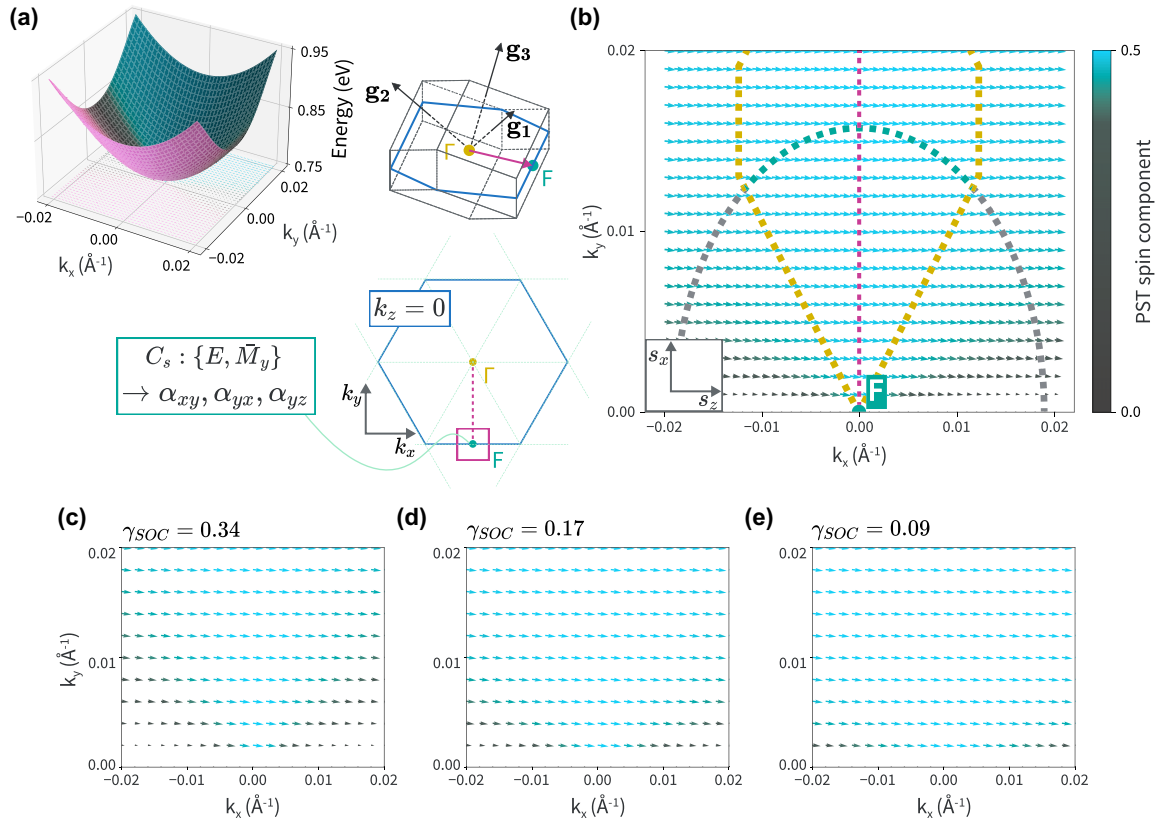

FIG. 3. (a) The lowest conduction band of Ag_3AsS_3 in the $k_z = 0$ plane in the Brillouin zone. The full Brillouin zone and the $k_z = 0$ plane are shown to the right with the $F \to \Gamma$ path highlighted. First-order SOC Hamiltonian terms in Eq. (3) are derived from the little group symmetries at the high-symmetry point of interest. (b) The spin texture of Ag_3AsS_3 showing a PST extending in the k_y direction along the $F \to \Gamma$ path. The spins are shown projected onto the $s_z - s_x$ plane. The color map indicates the spin component along the PST direction. The yellow-bordered region shows where the spin deviation is $<10^\circ$ from the PST direction and the elliptical region is the Fermi arc at a doping level of $n = 1 \times 10^{19}$ cm^{-3}. (c)–(e) The spin texture modeled with a two-band model [Eq. (3)] with varying values of Rashba anisotropy γ_{SOC}. Larger γ_{SOC} leads to a smaller PST region. (d) The model spin texture obtained using parameters fitted to the DFT data for Ag_3AsS_3.

highest occupied energy level (the VBM) and the lowest unoccupied energy level [the conduction band minimum (CBM)].

The MO diagram grants us insight into the chemical origin of the band gap: The interaction between the As and S atoms. If the orbital overlap is increased (decreased) between the p orbitals of the two species, we would expect the band gap to increase (decrease) due to further destabilization (stablization) of the antibonding orbitals. Since the proustite variants are isoelectronic and isostructural, the frontier orbitals are the same and we should expect the same mechanism to control the band gap. Figure 2(c) shows this linear dependence of the band gap on the As-S (or equivalent) bond length for each of the proustite variants, verifying this mechanism of band-gap control.

B. Spin texture

Figure 3(a) shows the the spin character of the lowest conduction band projected onto the $k_z = 0$ plane of the first Brillouin zone. We then use this projection to plot the spin texture of the conduction band near the F point in Fig. 3(b). We note that a mirror plane perpendicular to the $F \to \Gamma$ path intersects the F point, meaning the little group of the k vector at F is C_s. Based on Ref. [9], we expect a PST to occur along the mirror plane ($\hat{M}_y$) with spin locking along s_y. We find, however, a PST forming near the F point with spins aligned orthogonal to s_y centered along the $F \to \Gamma$ path and extending in the $\pm k_x$ directions. This PST is not symmetry protected and has another origin, which we explain below is accidental owing to anisotropy in the SOC strengths. We refer to the $F \to \Gamma$ path as the PST path and the orthogonal path along the mirror plane as the $F + k_x$ path. In addition to the unexpected direction of the PST path, we observe a small region on either side of the $F + k_x$ path where the spin deviates from the dominant PST direction (see color scale). The dominant PST spin orientation has normalized spin components $(-0.069, 0.495)$, given as an ordered pair (s_x, s_z); this oblique PST direction relative to the reciprocal lattice vectors is also unusual compared to previously reported bulk PST materials.

C. Two-band model

We now perform a symmetry analysis of the band structure of proustite near the F point to describe the SOC characteristics and attain a better understanding of the origin of the PST. Proustite exhibits $R3c$ symmetry and the little group of the F point is C_s, i.e., the only symmetry operators are the identity

TABLE III. Polarization (P), SOC parameters (α_{ij}, γ_{SOC}), and PSH properties (length l_{PSH} and period T_{PSH}) for proustite and its variants. The Rashba anisotropy γ_{SOC} is the ratio of the coupling strength along x to that along y. A smaller (more pronounced) Rashba anisotropy is favorable to PST formation and larger spin lifetime. Ag_3AsSe_3 has no computed spin lifetime (τ_s), indicated by N/A, because its conduction band minimum lies outside the PST region, making it practically inaccessible.

Material	P (μC cm^{-2})	α_{xy}(eV Å)	α_{yx} (eV Å)	α_{yz} (eV Å)	γ_{SOC}	l_{PSH} (nm)	τ_s (ps)	τ_s/T_{PSH}
Ag_3AsS_3	71.9	0.195	0.155	−1.12	0.173	231	2.00	3.18
Ag_3AsSe_3	109	0.210	1.192	1.81	0.0972	N/A	N/A	N/A
Ag_3SbS_3	65.1	0.166	0.539	−1.92	0.0833	148	3.69	21.7

and mirror plane: $\{E, \hat{\mathrm{M}}_y\}$. Following previous symmetry analyses [6,7], we construct a two-band model by applying symmetry constraints to obtain a first-order SOC Hamiltonian, with the F point as the origin:

$$\mathcal{H}_{\mathrm{SOC}} = \alpha_{xy}k_x\sigma_y + \alpha_{yx}k_y\sigma_x + \alpha_{yz}k_y\sigma_z. \quad (3)$$

Equation (3) allows us to immediately discern how the observed spin-momentum locking results along the $F \to \Gamma$ and $F + k_x$ paths. Along the $F + k_x$ path, $k_y = 0$ and the only relevant term couples k_x with σ_y, which explains the locking of the spin direction along the s_y axis on this path. Along the $F \to \Gamma$ path, $k_x = 0$ and the relevant terms couple k_y to both σ_x and σ_z, explaining the oblique spin texture along this path.

We assume that the full Hamiltonian describing the system near the CBM takes the form $\mathcal{H} = \mathcal{H}_0 + \mathcal{H}_{\mathrm{SOC}}$, with $\mathcal{H}_{\mathrm{SOC}}$ given by Eq. (3) and $\mathcal{H}_0$ being the free electron Hamiltonian, $\mathcal{H}_0 = \hbar^2k^2/2m^*$. Although $\mathcal{H}_0$ is a poor approximation of the real system as a whole, the approximation holds utility as an analytic tool to understand the mechanisms of the PST in proustite since the CBM can be locally approximated as parabolic. Since the Hamiltonian is quadratic in k and is otherwise only dependent on system-specific parameters, the Schrödinger equation can be solved analytically to give the following eigenvalues:

$$E_{\pm}(k) = \mathcal{H}_0 \pm \sqrt{(\alpha_{xy}k_x)^2 + (\alpha_{yx}k_y)^2 + (\alpha_{yz}k_y)^2}. \quad (4)$$

Along each $F \to \Gamma$ and $F + k_x$ path, one of the momentum components k_i is zero and the energy dispersion takes the form of a simple parabola with a linear coupling term. We can also solve for the eigenstates and their corresponding spin expectation values; by doing so, we are able to fit the computed DFT data to extract the α_{ij} coupling coefficients. With these values, we plot the resulting spin textures to assess whether the model reproduces the DFT-simulated PST [15]. Table III presents the α_{ij} values obtained by fitting to the DFT data about the F point. We define an effective $\alpha_{y,\mathrm{eff}} = (\alpha_{yx}^2 + \alpha_{yz}^2)^{1/2}$ to describe the net SOC band shift along k_y and note that there is an order of magnitude difference between the SOC coupling strengths along k_x and along k_y. This variation explains the dominance of the spin texture along k_y and the accidental origin of the PST. Because the SOC is much larger along the $F \to \Gamma$ path, the associated spin texture dominates the larger 2D region of the Brillouin zone.

We show the spin texture resulting from the two-band model with the fitted parameters in Fig. 3(d). We see that the first-order approximation fits the computed spin texture well in the region close to the F point. In Figs. 3(c)–3(e), we vary the SOC parameters in the two-band model to show how the parameters affect the PST. We find that the PST is controlled by the ratio $\gamma_{\mathrm{SOC}} = \alpha_{xy}/\alpha_{y,\mathrm{eff}}$; this ratio is equivalent to the Rashba anisotropy identified in Ref. [9] as a predictor of PST quality in type-I PSTs. A high degree of Rashba anisotropy (small γ_{SOC}) leads to the suppression of the weakly coupled spin component which results in a large PST area. As $\gamma_{\mathrm{SOC}} \to 0$, we approach a perfect PST. $\gamma_{\mathrm{SOC}} = 1$ corresponds to a case with no anisotropy between the SOC parameters, and the model reproduces a Rashba or Dresselhaus type spin texture, which has no inherent PST character. We note that the scalar γ_{SOC} is not dependent on the PST direction and can be used to characterize SOC in any material. Thus, we have identified and further confirmed the first-order Rashba anisotropy as one of the key indicators of PST quality for non-symmetry-protected PSTs.

It is of particular interest that the Rashba anisotropy is an effective predictor of PST areas in both type-I symmetry-protected PSTs, such as in Ref. [9], and type-II accidental PSTs, as in this paper. This finding blurs the lines between the current field of type-I and type-II PSTs, especially because if α_{xy} were to dominate the SOC Hamiltonian in Eq. (3), the resulting PST would be along a mirror plane and thus potentially be categorized as a type-I SP-PST. Consequently, the particular symmetries do not appear to dictate the quality of the PST, and instead the chemical interactions of the system and their interplay with the momentum-space physics determines the PST quality. This has been noted for some quasi-2D layered perovskite PSTs where the structural characteristics combine with the crystalline symmetries to constrain the relevant SOC terms to one in-plane direction, producing a PST which is occasionally labeled as symmetry protected. However, this type of symmetry protection is distinct from that of Ref. [6], in which symmetry constraints alone guarantee the existence of a PST near certain high-symmetry points. This strict symmetry requirement for defining SP-PSTs has been disputed [9] and is evidently too stringent for searching for new PST materials, as a multitude of materials without the strict symmetry protection have been shown to host a PST.

For these reasons, we propose a distinction between symmetry-*protected* PSTs in which symmetry guarantees a PST to first order and $\gamma_{\mathrm{SOC}} = 0$ exactly (e.g., $BiInO_3$ [6]) and symmetry-*assisted* PSTs in which symmetry reduces the number of first-order SOC terms such that structural or chemical features may force the system into a PST where $\gamma_{\mathrm{SOC}} \approx 0$ (e.g., layered perovskites [9,34]). The proustite PSTs presented here fit into the latter category, although there is a significant distinction in the PST formation mechanism in quasi-2D perovskites (see Ref. [34]) and the materials presented here. The layered perovskites exhibit PSTs due to

structural contraints—since the polarization is in-plane and the structure is quasi-2D, spin splitting occurs largely along one in-plane direction, producing a PST. In the 3D proustites, there is no intrinsic structural constraint. The large Rashba anisotropy forms exclusively through orbital interactions. Both cases, however, are notably distinct from true symmetry-protected PSTs by the fact that symmetry only plays a partial role in producing a symmetry-assisted PST.

Additionally, the result of our model is in contrast to the analysis presented in Ref. [7] for the layered perovskite $CsBiNb_2O_7$, where the *cubic* SOC splitting terms dominate and the anisotropy between those terms determines the PST quality. The difference in results can be explained by the difference in band dispersions. Since the PST in proustite is observed near the F point, the first-order expansion is sufficient to describe the PST near it. In $CsBiNb_2O_7$, the band extremum and associated PST is seen at large momentum, where higher order terms dominate and are thus necessary as part of the analysis.

D. Proustite variants

We now examine the two isostructural and isoelectronic proustite variants: Ag_3SbS_3 and Ag_3AsSe_3. Although they are chemically similar, there are significant changes in the SOC strengths. In addition, the location of the CBM changes drastically in Ag_3AsSe_3. Figure 4 shows the SOC band dispersions and PSTs of the conduction band of these variants; the corresponding SOC parameters are tabulated in Table III. The Rashba anisotropy is greatest in Ag_3SbS_3 followed by Ag_3AsSe_3. The PST areas outlined in yellow indicate regions within which the spin direction does not deviate from the PST beyond 10°; the larger the area with small spin deviation, the closer the PST is to ideal. We see that immediate to the F point ($k_y < 0.01\,\text{Å}^{-1}$), γ_{SOC} is a good predictor of PST area—smaller γ_{SOC} leads to a larger area. In Ag_3AsSe_3, γ_{SOC} fails as a predictor of PST area, although the fraction of the Fermi arc in the PST region is still large. This failure of γ_{SOC} in predicting the PST area is likely due to large cubic contributions to the SOC Hamiltonian as in $CsBiNb_2O_7$ [7]. This again suggests that first-order terms are insufficient to fully describe the PST in all materials, particularly those where the band minimum lies far from a high-symmetry point.

An important note is the location of the CBM. The PST states must lie at the CBM since they are transport states which need to be electron doped to access. While the band structure shown suggests that the CBM of Ag_3AsSe_3 lies within the $F \to \Gamma$ path, it is rather located in the $\Gamma \to$ M $(\frac{1}{3}, -\frac{2}{3}, \frac{1}{3})$ path, which is along a mirror plane (Fig. 5). Along this $\Gamma \to M$ path, however, there is no PST. The CBM seen in the $F \to \Gamma$ path is nearly degenerate with the true CBM. While these PST states are accessible through doping, most of the states within the donut-shaped Fermi surface are not PST states (Fig. 6). Thus, Ag_3AsSe_3 does not have a practically accessible PST.

The PSTs of the proustite variants confirm that the first-order Rashba anisotropy is a predictor of PST quality in materials where the CBM lies near the high-symmetry point. We further confirm this by computing the spin lifetime τ_s of the resulting PSH and the ratio of spin lifetime to the PSH

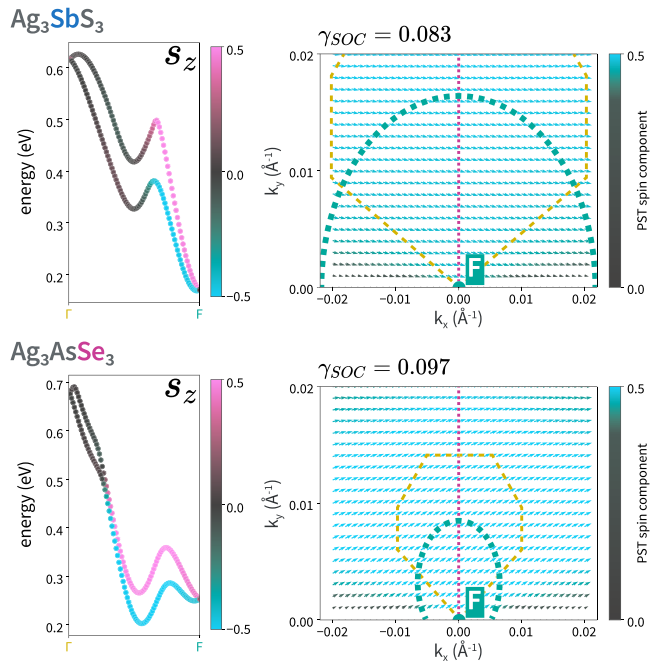

FIG. 4. The (left) s_z-projected conduction band and (right) spin textures of Ag_3SbS_3 and Ag_3AsSe_3 near the F point. The spins are shown projected onto the $s_z - s_x$ plane, and the color map indicates the spin component along the PST direction. The yellow-bordered region shows where the spin deviation is $<10°$ from the PST direction and the green-bordered region is the Fermi arc at a doping level of $n = 1 \times 10^{19}\,\text{cm}^{-3}$. Both variants display PSTs with Ag_3SbS_3 possessing a significantly greater PST area compared to Ag_3AsS_3. In the case of Ag_3AsSe_3, the CBM shifts due to bands shifting to lower energy along both the $F \to \Gamma$ path and the $\Gamma \to M$ (1/3, −2/3, 1/3) paths (Fig. 5); these two-band minima are nearly degenerate within ∼10 meV of each other. Consequently, the PST is inaccessible in Ag_3AsSe_3.

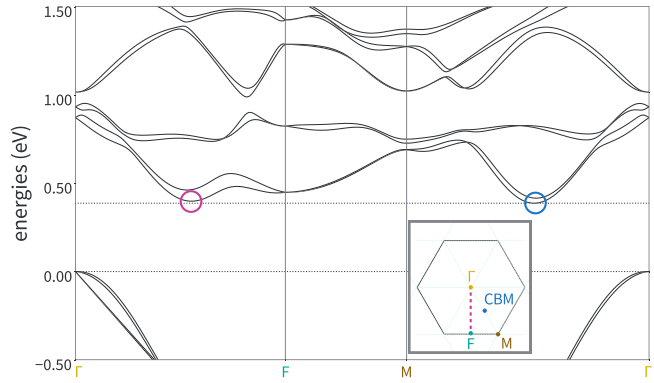

FIG. 5. Band structure of Ag_3AsSe_3 showing the $F \to \Gamma$ path as well as the true conduction band minimum (CBM) in the $\Gamma \to M$ path, circled in blue. The local CBM in the $F \to \Gamma$ path is circled in pink and the PST near this point is shown in Fig. 6. Inset: $k_z = 0$ slice of the Brillouin zone of Ag_3AsSe_3 showing the high-symmetry points of the band path. The M point, which is not part of standardized k-point paths for the $R3c$ space group, has C_{3v} point-group symmetry.

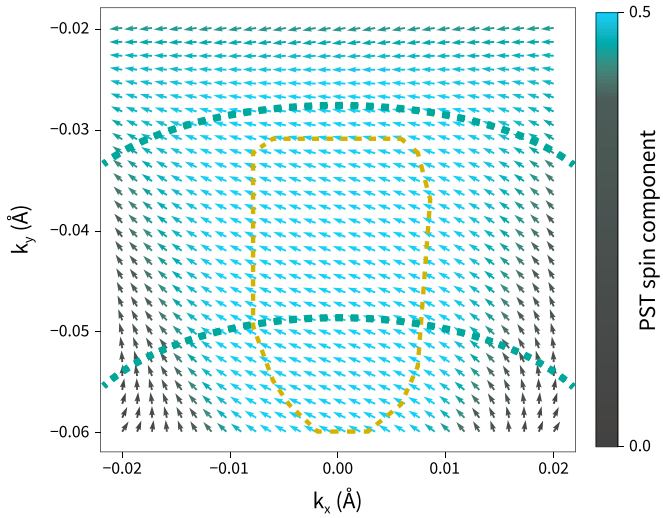

FIG. 6. PST of Ag_3AsSe_3 near the local CBM in the $F \rightarrow \Gamma$ path, circled in pink in Fig. 5. The spins are shown projected onto the $s_z - s_x$ plane, and the color map indicates the spin component along the PST direction. The yellow-bordered region shows where the spin deviation is $<10^\circ$ from the PST direction and the green-bordered region is the Fermi arc at a doping level of $n = 1 \times 10^{19}$ cm^{-3}.

period, which is a limiting factor in the material's device application potential (see Ref. [32] for details). We see that in the proustite family, Ag_3SbS_3 has the longest spin lifetime (3.69 ps) and τ_s/T_{PSH} ratio (21.7). However, compared to recently predicted bulk PST materials, these quantities are 1–3 orders of magnitude smaller and may require further engineering to find practical use [9]. For Ag_3AsSe_3, the location of the band minimum prevents the two-band model from fully describing the PST and therefore we do not compute the spin lifetime using the first-order model.

We also recognize the necessity of finding appropriate dopants to access the PST states. The PST states lie in the conduction band, so *n*-type doping is needed to access the PSH transport mode. One possible route to doping could be through vacancies on the chalcogenide site as in MoS_2 [35]. Photodoping could also be used to probe the PST states by utilizing circularly polarized light to excite electrons into the spin-polarized bands [34]. Finally, a two-dimensional electron gas (2DEG) may be achieved via interfacial doping or modulation doping [36], which would allow for direct verification of the 2DEG model we used to compute the spin lifetime.

IV. CONCLUSION

Although recent research into 3D bulk PST compounds has focused on PSTs formed by specific crystalline symmetries, such as the C_{2v} point group, we showed that such symmetries are unnecessary constraints in the search for new PST materials. We showed that the proustite mineral family offers a flexible platform to design structural and electronic properties, including tuning the low-symmetry PST in the conduction band. We also distinguished symmetry-*assisted* PSTs from symmetry-*protected* PSTs, categorizing the majority of previously identified PST materials along with the proustites as symmetry-assisted PSTs. We propose that the Rashba anisotropy γ_{SOC} is a useful parameter in evaluating PSTs near a high-symmetry k vector and that this concept may be extended to higher orders. We conjecture that high Rashba anisotropy at multiple orders could result in an ideal PST that spans a significant portion of the Brillouin zone. We propose that this Rashba anisotropy criterion could be used in high-throughput screening of materials for future bulk PST identification in a manner similar to searches for novel Rashba materials [37]. Since symmetry does not present a strong constraint on the existence of bulk PSTs, there may be several unexplored material classes in which PSTs are hidden. In addition, future work into studying the fundamental mechanisms of PSTs should focus on the chemical and structural origins of the Rashba anisotropy, as this is still unclear. Understanding how to control this Rashba anisotropy may be the key to unlocking full design and performance optimization of PST materials.

ACKNOWLEDGMENTS

S.K. thanks Dr. X.-Z. Lu for his guidance and many stimulating discussions. This research was supported by the National Science Foundation (NSF) under Award No. DMR-2104397. Computational resources were provided by the Quest high performance computing facility at Northwestern University, which is jointly supported by the Office of the Provost, the Office for Research, and Northwestern University Information Technology; Stampede2 at the Extreme Science and Engineering Discovery Environment (XSEDE), funded by the NSF through Award No. ACI-1540931; and Carbon at the Center for Nanoscale Materials, a U.S. Department of Energy Office of Science User Facility, supported by the U.S. DOE, Office of Basic Energy Sciences, under Contract No. DE-AC02-06CH11357.

[1] B. A. Bernevig, J. Orenstein, and S.-C. Zhang, Exact SU(2) Symmetry and Persistent Spin Helix in a Spin-orbit Coupled System, Phys. Rev. Lett. **97**, 236601 (2006).

[2] J. Schliemann, Colloquium: Persistent spin textures in semiconductor nanostructures, Rev. Mod. Phys. **89**, 011001 (2017).

[3] J. D. Koralek, C. P. Weber, J. Orenstein, B. A. Bernevig, S.-C. Zhang, S. Mack, and D. D. Awschalom, Emergence of the persistent spin helix in semiconductor quantum wells, Nature (London) **458**, 610 (2009).

[4] M. A. U. Absor, Y. Faishal, M. Anshory, I. Santoso, and F. Ishii, Highly persistent spin textures with giant tunable spin splitting in the two-dimensional germanium monochalcogenides, J. Phys.: Condens. Matter **33**, 305501 (2021).

[5] N. Yamaguchi and F. Ishii, Strain-induced large spin splitting and persistent spin helix at $LaAlO_3/SrTiO_3$ interface, Appl. Phys. Express **10**, 123003 (2017).

[6] L. L. Tao and E. Y. Tsymbal, Persistent spin texture enforced by symmetry, Nat. Commun. **9**, 2763 (2018).

[7] C. Autieri, P. Barone, J. Sławińska, and S. Picozzi, Persistent spin helix in Rashba-Dresselhaus ferroelectric $CsBiNb_2O_7$, Phys. Rev. Mater. **3**, 084416 (2019).

[8] H. Djani, A. C. Garcia-Castro, W.-Y. Tong, P. Barone, E. Bousquet, S. Picozzi, and P. Ghosez, Rationalizing and engineering Rashba spin-splitting in ferroelectric oxides, npj Quantum Mater. **4**, 51 (2019).

[9] X.-Z. Lu and J. M. Rondinelli, Discovery principles and materials for symmetry-protected persistent spin textures with long spin lifetimes, Matter **3**, 1211 (2020).

[10] L. L. Tao and E. Y. Tsymbal, Perspectives of spin-textured ferroelectrics, J. Phys. D **54**, 113001 (2021).

[11] X.-Z. Lu and J. M. Rondinelli, Strain engineering a persistent spin helix with infinite spin lifetime, Phys. Rev. B **107**, 035155 (2023).

[12] K. A. Schönau and S. A. T. Redfern, High-temperature phase transitions, dielectric relaxation, and ionic mobility of proustite, Ag_3AsS_3, and pyrargyrite, Ag_3SbS_3, J. Appl. Phys. **92**, 7415 (2002).

[13] P. J. S. Ewen, W. Taylor, and G. L. Paul, A Raman scattering study of phase transitions in proustite (Ag_3AsS_3) and pyrargyrite (Ag_3SbS_3), J. Phys. C: Solid State Phys. **16**, 6475 (1983).

[14] K. Kihara and T. Matsumoto, Refinements of Ag_3AsSe_3 based on high-order thermal-motion tensors, Z. Kristallogr. Cryst. Mater **177**, 211 (1986).

[15] S. Koyama and J. M. Rondinelli, Proustite PST Data and Code (2023), https://github.com/MTD-group/proustites-pst.

[16] G. Kresse and J. Hafner, *Ab initio* molecular dynamics for liquid metals, Phys. Rev. B **47**, 558 (1993).

[17] G. Kresse and J. Furthmüller, Efficient iterative schemes for *ab initio* total-energy calculations using a plane-wave basis set, Phys. Rev. B **54**, 11169 (1996).

[18] G. Kresse and J. Furthmüller, Efficiency of *ab-initio* total energy calculations for metals and semiconductors using a plane-wave basis set, Comput. Mater. Sci. **6**, 15 (1996).

[19] G. Kresse and D. Joubert, From ultrasoft pseudopotentials to the projector augmented-wave method, Phys. Rev. B **59**, 1758 (1999).

[20] P. E. Blöchl, Projector augmented-wave method, Phys. Rev. B **50**, 17953 (1994).

[21] J. P. Perdew, K. Burke, and M. Ernzerhof, Generalized Gradient Approximation Made Simple, Phys. Rev. Lett. **77**, 3865 (1996).

[22] J. P. Perdew, A. Ruzsinszky, G. I. Csonka, O. A. Vydrov, G. E. Scuseria, L. A. Constantin, X. Zhou, and K. Burke, Restoring the Density-gradient Expansion for Exchange in Solids and Surfaces, Phys. Rev. Lett. **100**, 136406 (2008).

[23] P. E. Blöchl, O. Jepsen, and O. K. Andersen, Improved tetrahedron method for Brillouin-zone integrations, Phys. Rev. B **49**, 16223 (1994).

[24] R. D. King-Smith and D. Vanderbilt, Theory of polarization of crystalline solids, Phys. Rev. B **47**, 1651 (1993).

[25] A. V. Krukau, O. A. Vydrov, A. F. Izmaylov, and G. E. Scuseria, Influence of the exchange screening parameter on the performance of screened hybrid functionals, J. Chem. Phys. **125**, 224106 (2006).

[26] A. Hjorth Larsen, J. Jørgen Mortensen, J. Blomqvist, I. E. Castelli, R. Christensen, M. Dułak, J. Friis, M. N. Groves, B. Hammer, C. Hargus, E. D. Hermes, P. C. Jennings, P. Bjerre Jensen, J. Kermode, J. R. Kitchin, E. Leonhard Kolsbjerg, J. Kubal, K. Kaasbjerg, S. Lysgaard, J. Bergmann Maronsson *et al.*, The atomic simulation environment—a Python library for working with atoms, J. Phys.: Condens. Matter **29**, 273002 (2017).

[27] R. Dronskowski and P. E. Bloechl, Crystal orbital Hamilton populations (COHP): Energy-resolved visualization of chemical bonding in solids based on density-functional calculations, J. Phys. Chem. **97**, 8617 (1993).

[28] V. L. Deringer, A. L. Tchougréeff, and R. Dronskowski, Crystal orbital Hamilton population (COHP) analysis as projected from plane-wave basis sets, J. Phys. Chem. A **115**, 5461 (2011).

[29] S. Maintz, V. L. Deringer, A. L. Tchougréeff, and R. Dronskowski, Analytic projection from plane-wave and PAW wave functions and application to chemical-bonding analysis in solids, J. Comput. Chem. **34**, 2557 (2013).

[30] S. Maintz, V. L. Deringer, A. L. Tchougréeff, and R. Dronskowski, LOBSTER: A tool to extract chemical bonding from plane-wave based DFT, J. Comput. Chem. **37**, 1030 (2016).

[31] K. Momma and F. Izumi, *VESTA 3* for three-dimensional visualization of crystal, volumetric and morphology data, J. Appl. Cryst. **44**, 1272 (2011).

[32] X. Liu and J. Sinova, Unified theory of spin dynamics in a two-dimensional electron gas with arbitrary spin-orbit coupling strength at finite temperature, Phys. Rev. B **86**, 174301 (2012).

[33] V. Y. Rud, Y. V. Rud, and E. I. Terukov, Development and photoelectric properties of In/*p*-Ag_3AsS_3 surface-barrier structures, Semiconductors **44**, 1025 (2010).

[34] L. Zhang, J. Jiang, C. Multunas, C. Ming, Z. Chen, Y. Hu, Z. Lu, S. Pendse, R. Jia, M. Chandra, Y.-Y. Sun, T.-M. Lu, Y. Ping, R. Sundararaman, and J. Shi, Room-temperature electrically switchable spin-valley coupling in a van der Waals ferroelectric halide perovskite with persistent spin helix, Nat. Photonics **16**, 529 (2022).

[35] P.-C. Shen, Y. Lin, C. Su, C. McGahan, A.-Y. Lu, X. Ji, X. Wang, H. Wang, N. Mao, Y. Guo, J.-H. Park, Y. Wang, W. Tisdale, J. Li, X. Ling, K. E. Aidala, T. Palacios, and J. Kong, Healing of donor defect states in monolayer molybdenum disulfide using oxygen-incorporated chemical vapour deposition, Nat. Electron. **5**, 28 (2022).

[36] A. Zunger and O. I. Malyi, Understanding doping of quantum materials, Chem. Rev. **121**, 3031 (2021).

[37] C. M. Acosta, E. Ogoshi, A. Fazzio, G. M. Dalpian, and A. Zunger, The Rashba scale: Emergence of band anti-crossing as a design principle for materials with large Rashba coefficient, Matter **3**, 145 (2020).